PHYSICAL REVIEW B **94**, 235432 (2016)

Thin-film growth dynamics with shadowing effects by a phase-field approach

Marco Salvalaglio,[1,2,*] Rainer Backofen,[1] and Axel Voigt[1,3]
[1] *Institute of Scientific Computing, Technische Universität Dresden, 01062 Dresden, Germany*
[2] *IHP, Im Technologiepark 25, 15236 Frankfurt (Oder), Germany*
[3] *Dresden Center for Computational Materials Science (DCMS), TU Dresden, 01062 Dresden, Germany*

(Received 15 September 2016; published 23 December 2016)

Shadowing effects during the growth of nano- and microstructures are crucial for the realization of several technological applications. They are given by the shielding of the incoming material flux provided by the growing structures themselves. Their features have been deeply investigated by theoretical approaches, revealing important information to support experimental activities. However, comprehensive investigations able to follow every stage of the growth processes as a whole, particularly useful to design and understand targeted experiments, are still challenging. In this work, we study the thin-film growth dynamics by means of a diffuse interface approach accounting for both deposition with shadowing effects and surface diffusion driven by the minimization of the surface energy. In particular, we introduce the coupling between a phase-field model and the detailed calculation of the incoming material flux at the surface deposited from vacuum or vapor phase in the ballistic regime. This allows us to finely reproduce the realistic morphological evolution during the growth on nonflat substrates, also accounting for different flux distributions. A general assessment of the method, focusing on two-dimensional profiles, is provided thanks to the comparison with a sharp-interface approach for the evolution of the early stages. Then, the long-time-scale dynamics is shown in two and three dimensions, providing a general overview of the features observed during deposition on corrugated surfaces involving flattening, increasing of surface roughness with the growth of columnar structures, and voids formation.

DOI: 10.1103/PhysRevB.94.235432

I. INTRODUCTION

The investigation of the morphological evolution during the growth of crystalline thin films is crucial in order to optimize the outcome of experiments tailoring material properties. Indeed, such processes may be finely tuned leading, for instance, to the formation of self-assembled nanostructures [1,2] and/or to peculiar morphologies with a high degree of ordering thanks to the patterning of the substrate [3]. Deeply patterned substrates can be also adopted in order to move from planar to three-dimensional crystal growth [4].

The growth dynamics of thin films can be generally described within continuum approaches. This kind of modeling is highly demanded as it allows for the description of the typical time and length scales observed in experiments, not accessible with atomistic approaches [5–7]. Usually, continuum models account for local properties only, e.g., for the local chemical potential [5]. However, in order to describe growth processes like sputtering or glancing angle deposition [8,9], nonlocal effects due to the ballistic shadowing have to be considered. During sputtering deposition, for instance, the growth velocity due to the incorporation of material in the solid phase is expected to be proportional to the effective exposure angle θ at the surface as shown in Fig. 1 [10,11]. Any undulation due to the inherent surface roughness would then lead to inhomogeneities in the growth velocity as local peaks collect more material than the valleys. As a result, the surface roughness increases during growth, resulting in the so-called shadowing instability [10,12–14]. This strictly holds true when material redistribution at the surface is negligible. If not, as for instance during deposition at high temperatures, surface diffusion plays an important role and a different behavior can be observed [11]. Indeed, this mechanism leads to the flattening of wavy profiles according to surface energy minimization [15,16], thus representing a competitive mechanism with respect to the shadowing instability itself. The growth of peculiar morphology as networks of columnar structures and voids has been already explained accounting for the simultaneous occurrence of these phenomena [11,17]. Moreover, these effects are generally found to be crucial for explaining the outcomes of the deposition on deeply patterned substrates [4,18,19].

The investigation of crystal growth from a vapor phase and/or under vacuum including shadowing has been carried out by several different approaches as sharp interface, continuum modeling (see, e.g., Refs. [10,11,20,21]), and also by means of discrete modeling with Monte Carlo sampling of the incoming material flux (see, e.g., Refs. [13,22–25]). Within these approaches, the main features of the morphological evolution were described and scaling laws for the thin-film growth dynamics were predicted [26]. However, they do not generally cope with the complexity of real systems. A remarkable procedure, able to describe shadowing effects in detail for etching, deposition, and lithography has been introduced within a level set approach [27,28]. By means of a similar approach, a Monte Carlo ray-tracing procedure has been used to describe etching processes in Ref. [29]. These models allow most of the physics behind shadowing effects to be described, but they are difficult to be used for the full modeling of nano- and microstructures growth on flat and patterned substrates, in particular when considering other important contributions to the evolution [7].

Phase-field (PF) models play a prominent role in continuum modeling of materials [7,30–32]. Indeed, they allow

---

[*] marco.salvalaglio@tu-dresden.de

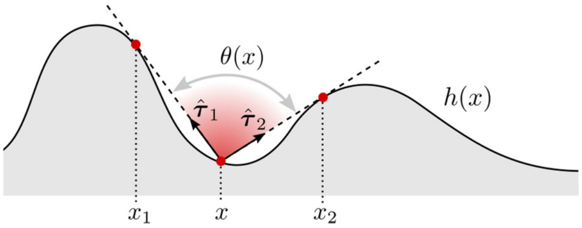

FIG. 1. Illustration of the exposure angle θ for a 2D profile $h(x)$. Only rays with an orientation between $\hat{\tau}_1$ and $\hat{\tau}_2$ can reach the surface in x. These vectors correspond to the tangent directions to $h(x)$ at $x = x_1$ and $x = x_2$, respectively.

differential equations describing the dynamics of specific systems to be solved for complex geometries, also naturally accounting for dramatic variations in the morphology with topological changes. Moreover, when dealing with the definition of the solid and vapor/vacuum phase, such PF models are effective in describing a lot of phenomena and features typically present in thin solid films, such as anisotropic surface energy minimization [33–35], evolution of elastically stressed films [36,37], alloying [38], and contact angles between the epilayer and the substrate [39]. Despite the versatility of the PF approaches, a comprehensive modeling of the growth in the ballistic regime including shadowing has not been introduced yet. This is mainly due to the nonlocal character of these effects, which generally requires us to know the coordinates of the surface profile, not easily accessible within the implicit description of the surface achieved with PF models.

In this work we provide an investigation of the thin-film growth dynamics focusing on the competition between the morphological evolution due to surface diffusion and deposition with shadowing effects. A convenient diffuse interface description of the material redistribution at the surface of the solid phase, driven by the minimization of the surface energy, is selected and it is coupled to a detailed modeling of the incoming material flux including the shielding provided by the surface profile itself. Thanks to this approach, several different regimes are investigated just by varying the simulation parameters and the features of the corresponding growth technique, such as the material flux distribution. Moreover, it can be easily extended to include other physical effects [7]. The PF model is briefly illustrated in Sec. II. Then the calculation of the effective material flux reaching the substrate is presented in Sec. III. In Sec. IV the early stage dynamics of simple, wavy profiles in 2D is analyzed by a sharp interface approach and it is compared to the outcome of PF simulations to provide a general assessment of the method. Then, the long time scale dynamics, deeply exploiting the advantages of the PF approach, is illustrated in Sec. V. Here the main features of the morphological evolution during deposition are outlined both in two and three dimensions (2D and 3D, respectively), unveiling the generality of the observed features and the capabilities of the method. Conclusions and remarks are summarized in Sec. VI.

II. PHASE-FIELD MODEL

The approach adopted in this work consists of evaluating the evolution in time of an order parameter φ which describes the solid ($\varphi = 1$) and the vacuum ($\varphi = 0$) phase, with a continuous variation in between. The model is based on the standard definition of the Ginzburg-Landau energy functional

$$G = \int_\Omega \gamma \left(\frac{\epsilon}{2} |\nabla \varphi|^2 + \frac{1}{\epsilon} B(\varphi) \right) d\mathbf{x}. \tag{1}$$

Ω represents the entire domain where $\varphi(\mathbf{x})$ is defined, ϵ is the interface thickness between the two phases, and $B(\varphi) = 18\varphi^2(1-\varphi)^2$ [31]. For the sake of simplicity, the surface energy density γ is assumed to be isotropic with $\gamma = 1$. A general extension of the model to anisotropic surface energies can be found in Refs. [33,34]. The evolution law is then given by

$$\frac{\partial \varphi}{\partial t} = \nabla \cdot [M(\varphi) \nabla \mu] + \Phi |\nabla \varphi|, \tag{2}$$

where the first term describes the diffusion along the surface with $\mu = \delta G / \delta \varphi$ the chemical potential, and the second term accounts for the incoming material flux density Φ producing the growth of the solid phase. $M(\varphi) = (36/\epsilon)\varphi^2(1-\varphi^2)$ is the mobility function restricted to the surface [31]. The equation for μ reads

$$g(\varphi)\mu = -\epsilon\gamma\nabla^2\varphi + \frac{1}{\epsilon}\gamma B'(\varphi). \tag{3}$$

$g(\varphi) = 30\varphi^2(1-\varphi^2)$ is included to ensure higher order convergence in the limit $\epsilon \to 0$ [36,40,41]. According to the minimization of the energy functional of Eq. (1), the profile in the direction perpendicular to the interface is well described by

$$\varphi(\mathbf{x}) = \frac{1}{2}\left[1 - \tanh\left(\frac{3d(\mathbf{x})}{\epsilon}\right)\right], \tag{4}$$

with $d(\mathbf{x})$ is the signed distance from the surface of the solid phase [31]. An illustration of the PF representation of a generic profile is reported in Fig. 2(a).

For deposition techniques and/or substrates which produce a uniform incoming material flux at the surface, Φ is a constant. In order to account for shadowing effects, Φ should be described by a function of spatial coordinates and it is defined as

$$\Phi(\mathbf{x}) = F\mathcal{S}(\mathbf{x}), \tag{5}$$

where the shadowing function $\mathcal{S}(\mathbf{x})$ is a non-negative function describing the shielding of the incoming material flux. That is, $\mathcal{S}(\mathbf{x})$ is the amount of the total flux F that reaches $\mathbf{x}$. $\mathcal{S}(\mathbf{x})$ is chosen to be constant in the direction perpendicular to the interface. Mass conservation of incoming flux leads to a normalization condition:

$$\int_\Omega \mathcal{S}(\mathbf{x})|\nabla\varphi(\mathbf{x})| d\mathbf{x} = 1. \tag{6}$$

Notice that when shadowing effects are negligible, the $\mathcal{S}(\mathbf{x})$ distribution should be constant at the surface. In Sec. III the ray-tracing algorithm for the evaluation of this function on a generic profile defined by φ is reported. The simulations shown in this work are obtained by integrating Eqs. (2) and (3) using the adaptive finite element toolbox AMDiS [42,43] with a semi-implicit integration scheme and mesh refinement at the interface as in Ref. [34].

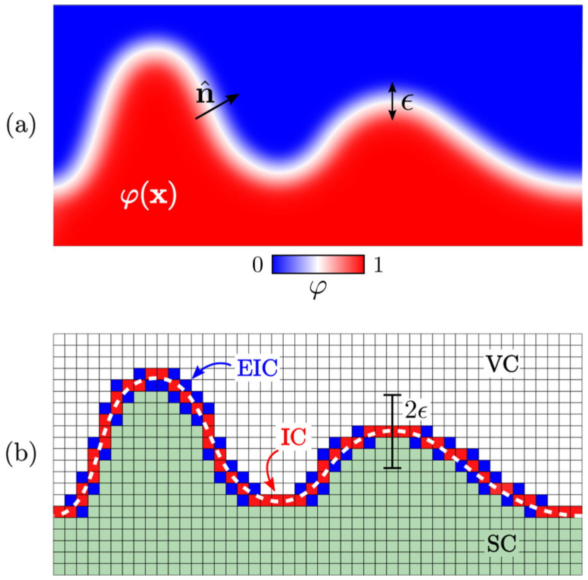

FIG. 2. Coupling of PF model and flux shielding algorithm. (a) Generic 2D profile resembling the one in Fig. 1 defined within the PF framework by $\varphi(\mathbf{x})$. The interface thickness ϵ and the outer-pointing surface normal $\hat{\mathbf{n}}$ are also shown. (b) Definition of the cells in the regular grid for the calculation of the incoming material flux at the surface. The dashed white line corresponds to the $\varphi \sim 0.5$ isoline of (a). The solid black line illustrates the region where the value of $\mathcal{S}$ are extended to be used in Eq. (2).

III. FLUX SHIELDING ALGORITHM

We use a ray-tracing algorithm [44,45] in order to model the source and the self-shadowing of the growth front. A point, namely a dimensionless particle, with a prescribed evolution direction represents a ray as, e.g., in Ref. [29]. The initial position and direction distribution of the particles describe the characteristics of the source of material. Then the amount of particles reaching some part of the surface defines the local flux density at the surface and thus the local growth velocity. In order to efficiently track the particle impingement at the surface, the interface between phases is first represented on a regular grid as illustrated in Fig. 2(b). All the cells where $\varphi > 0.5$ are set to be solid (solid cells, SC) and the other cells to vacuum (vacuum cells, VC). The interface is defined by SC with at least one VC as nearest neighbor [46]. For later use we also define extended interface cells (EIC). EIC are SC (VC) with at least one next-nearest neighbor cell which is VC (SC) but not an IC. The ray-tracing particles are then propagated along their predefined direction and collected in the first IC they arrive. It is worth mentioning that the PF model is not able to resolve any length scale smaller than the interface thickness [31]. So that values of $\mathcal{S}$ are averaged over a number of boundary cells given by the ratio between ϵ and the length of the side of the squared cells in the regular grid Δx. According to this, we select $\Delta x = \epsilon/n$ with n an integer number and $n \geqslant 2$. In this work we select $n = 8$ and $n = 4$ for 2D and 3D simulations, respectively. Normalized by the total number of ray-tracing particles, chosen to provide the proper sampling of the surface, $\mathcal{S}$ defines the value of shadowing in an interface cell, namely $\mathcal{S}(\mathrm{IC})$. In order to apply this in the evolution law, given by Eq. (2), $\mathcal{S}(\mathbf{x})$ has to be defined in the entire interfacial region, i.e., where $|\nabla\varphi| > 0$. In a first step, $\mathcal{S}(\mathbf{x})$ is defined in the EIC as an average of its values in the neighboring ICs. Second, in the interface region, $\mathcal{S}(\mathbf{x})$ is extended in the direction normal to the interface by solving [47]

$$\nabla\mathcal{S}(\mathbf{x}) \cdot \hat{\mathbf{n}} = 0. \tag{7}$$

$\hat{\mathbf{n}} = -\nabla\varphi/|\nabla\varphi|$ is the outer-pointing normal to the interface, as illustrated in Fig. 2(a). The extension is performed in a region with a thickness equal to 2ϵ as illustrated in Fig. 2(b). The interpolation of $\mathcal{S}(\mathbf{x})$ back to the locally refined unstructured mesh used to solve the equations of Sec. II is straightforward and, thus, Eq. (2) is well defined. The whole algorithm can be summarized as follows:

(1) Define the interface on a regular grid.

(2) Collect the ray-tracing particles in ICs and calculate $\mathcal{S}(\mathrm{IC})$.

(3) Extend $\mathcal{S}$ in the direction perpendicular to interface: $\mathcal{S}(\mathrm{IC}) \rightarrow \mathcal{S}(\mathbf{x})$.

(4) Interpolate to the unstructured finite element mesh.

(5) Solve the evolution law given by Eq. (2).

$\mathcal{S}(\mathbf{x})$ is a function of the distribution of ray-tracing particles. Thus, a variety of different sources can be modeled. Isotropic sources are modeled by choosing initial particles evenly distributed in space far away from the surface with random directions. Directional fluxes, e.g., mimicking glancing-angle deposition, are modeled by restricting the motion of particles to a preferred direction. Source location and geometries are directly modeled by the initial distribution in space of the ray-tracing particles. Even additional features like reflection or scattering [25] may be easily included in this algorithm by allowing for changes in the direction during the ray tracing of a single particle and by introducing an incorporation rate for particles reaching the surface. In this work, we focus on the deposition in the ballistic regime. However, the same procedure would apply also to other regimes, by accounting for the proper evolution of the particles.

The outcome of the aforementioned procedure is illustrated in Fig. 3 where $\bar{\mathcal{S}}(\mathbf{x})$, namely the $\mathcal{S}(\mathbf{x})|\nabla\varphi|$ distribution normalized by its maximum values, is shown for both 2D and 3D profiles with different incoming fluxes. The total number of the incoming particles is chosen large enough to ensure no variation in the $\mathcal{S}(\mathbf{x})$ when increasing the number of rays ($\sim 10^5$ in 2D and $\sim 10^6$ in 3D). The same applies to any simulation reported in the following. Figures 3(a)–3(d) show $\bar{\mathcal{S}}(\mathbf{x})$ values in the 2D simulation domain. In Figs. 3(e)–3(h) the values of this quantity are shown at the $\varphi \sim 0.5$ isosurfaces while the gray domains correspond to the solid phase, i.e., to the region with $\varphi > 0.5$. The initial condition for $\varphi(\mathbf{x})$ is set by means of Eq. (4) with $d(\mathbf{x})$ the signed distance from $h(x) = \pi R\cos(x) + h_0$ in 2D with $x \in [0,4\pi]$ and $h(x,y) = \pi R[\cos(x) + \cos(y)] + h_0$ in 3D with $x \in [0,4\pi]$ and $y \in [0,4\pi]$. Different values for R, namely the aspect ratio of the resulting profiles, are considered. Periodic boundary conditions in the in-plane directions ($\hat{\mathbf{x}}$ and $\hat{\mathbf{y}}$, the latter only in 3D) are set, along with no-flux boundary condition along the vertical direction. The same boundary conditions are adopted for all the other simulations of this work.

First, let us focus on the case of sputtering deposition, i.e., with particles generated randomly in the vacuum phase far

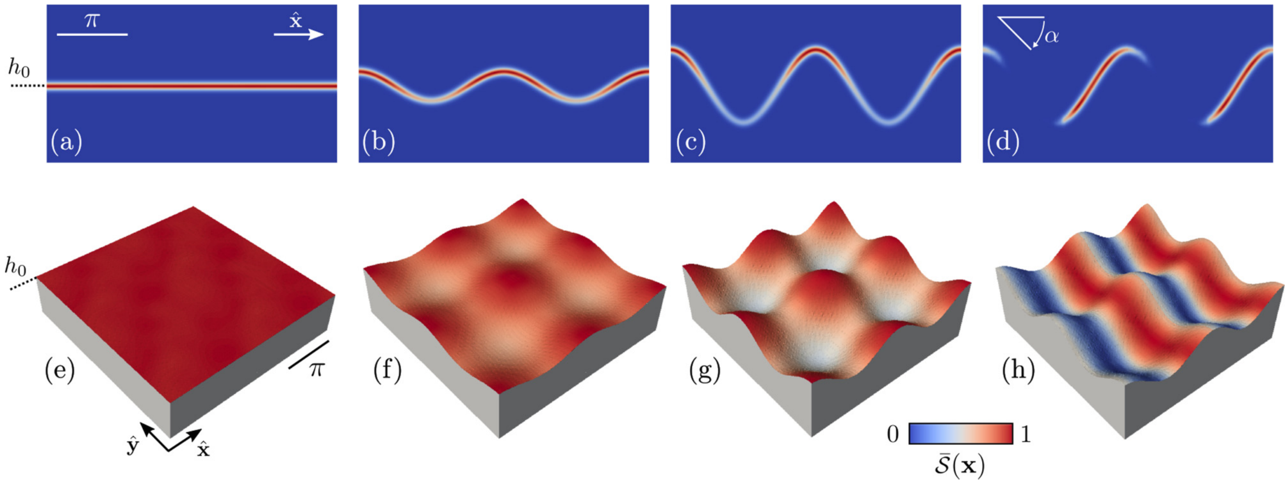

FIG. 3. Maps of the $\bar{\mathcal{S}}(\mathbf{x})$ distribution obtained by the flux-shielding algorithm on wavy profiles. (a)–(c) Results of sputtering deposition on 2D profiles with aspect ratio (R) values of 0.0, 0.2, and 0.5, respectively. (d) as in (c) with a prescribed direction $\alpha = -\pi/4$ for the incoming material flux (as illustrated in the panel). $\epsilon = \pi/5$ and $\Delta x = \epsilon/8$. (e)–(g) Results of sputtering deposition on 3D profiles with aspect ratio (R) values of 0.0, 0.2, and 0.5, respectively. (h) as in (g) with a prescribed direction for the incoming material flux with an angle of $-\pi/4$. $\epsilon = \pi/5$ and $\Delta x = \epsilon/4$.

away from the interface with random directions $\alpha \in]-\pi,0[$. According to the diffuse interface description, we obtained nonvanishing values of $\bar{\mathcal{S}}(\mathbf{x})$ only within the interface. For $R = 0$, the surface profile is flat and shadowing effects are not present. Indeed, a uniform flux distribution is obtained along the surface, i.e., no variation of the shadowing function $\mathcal{S}(\mathbf{x})$ is expected along φ isolines in 2D and isosurfaces in 3D as shown in Figs. 3(a) and 3(e), respectively. Then, by increasing R values, inhomogeneities of $\bar{\mathcal{S}}(\mathbf{x})$ appear with higher values at the peaks and lower values at the valleys as shown in Figs. 3(b) and 3(f) for $R = 0.2$. Such differences increase for larger R values as can be seen in Figs. 3(c) and 3(g) where $R = 0.5$. As discussed previously, the ray-tracing algorithm allows various features of deposition techniques to be considered. This is illustrated in Figs. 3(d) and 3(h). Different to the other cases, a directional deposition is considered there by randomly generating particles in the vacuum phase with a single orientation $\alpha = -\pi/4$. The result consists of an asymmetric $\bar{\mathcal{S}}(\mathbf{x})$ distribution which has maximum values where the rays can directly reach the surface and goes to zero when they are completely shielded. These effects are clearly observed during glancing angle deposition [8,9], resulting in the growth of tilted structures.

IV. EARLY STAGES OF DEPOSITION AND MODEL ASSESSMENT

We focus now on the first stages of the deposition on corrugated surfaces. The method introduced in Secs. II and III allows for the calculation of the velocity distribution on a selected profile and, thus, the evaluation of the expected evolution during deposition. Notice that in the very first stages of the growth process, in the regime where surface diffusion is active, dramatic changes in the geometries are not expected [17]. Therefore, once the initial profile is known, the velocity at the surface can be easily derived by other approaches involving the explicit description of the surface. In particular, this holds true for 2D profiles described by analytic functions. In this section, a sharp-interface approach is adopted to calculate the evolution of a surface profile during the first stages of deposition. Then, the results obtained thereby are compared to the outcome of PF simulations, assessing the reliability of the method introduced in the previous sections.

A. Sharp-interface approach

Let us consider a 2D, wavy profile described by a cosine function as in Fig. 4(a), given by

$$h(x) = A\cos(qx), \tag{8}$$

where A is the amplitude and q the wave number. $L = 2\pi/q$ defines the wavelength of the profile. The aspect ratio of the profile is given by $R = 2A/L$. By assuming an isotropic, unitary surface energy density, the evolution by surface diffusion in terms of the magnitude of the velocity along the outer-pointing surface normal is [15,16]

$$v_{\hat{\mathbf{n}}}^{\mathrm{d}}(x) = D\nabla_\Gamma^2\kappa(x), \tag{9}$$

with D the diffusion coefficient and κ the local curvature. The latter is given by $\kappa(x) = -h''(x)/\{1+[h'(x)]^2\}^{3/2}$. ∇_Γ^2 is the surface Laplacian along the surface profile Γ [48]. In Fig. 4(b) the $v_{\hat{\mathbf{n}}}^{\mathrm{d}}$ values are shown for three different values of R with $q = 1$ and $D = 1$.

In order to account for material flux during deposition, an additional term $v_{\hat{\mathbf{n}}}^{\mathrm{f}} = F\mathcal{S}(x)$ is considered and the evolution law then reads $v_{\hat{\mathbf{n}}} = v_{\hat{\mathbf{n}}}^{\mathrm{d}}(x) + v_{\hat{\mathbf{n}}}^{\mathrm{f}}(x)$. We focus here on the general case of sputtering deposition. Therefore, the flux shielding of the profile can be quantified by considering the effective exposure angle θ at the surface as illustrated in Fig. 4(a). The $\theta(x)$ distribution can be calculated as the angle between vectors $\hat{\boldsymbol{\tau}}_1$ and $\hat{\boldsymbol{\tau}}_2$ (see Fig. 1) as

$$\theta(x) = \arccos\left(\frac{\hat{\boldsymbol{\tau}}_1(x)\cdot\hat{\boldsymbol{\tau}}_2(x)}{|\hat{\boldsymbol{\tau}}_1(x)||\hat{\boldsymbol{\tau}}_2(x)|}\right). \tag{10}$$

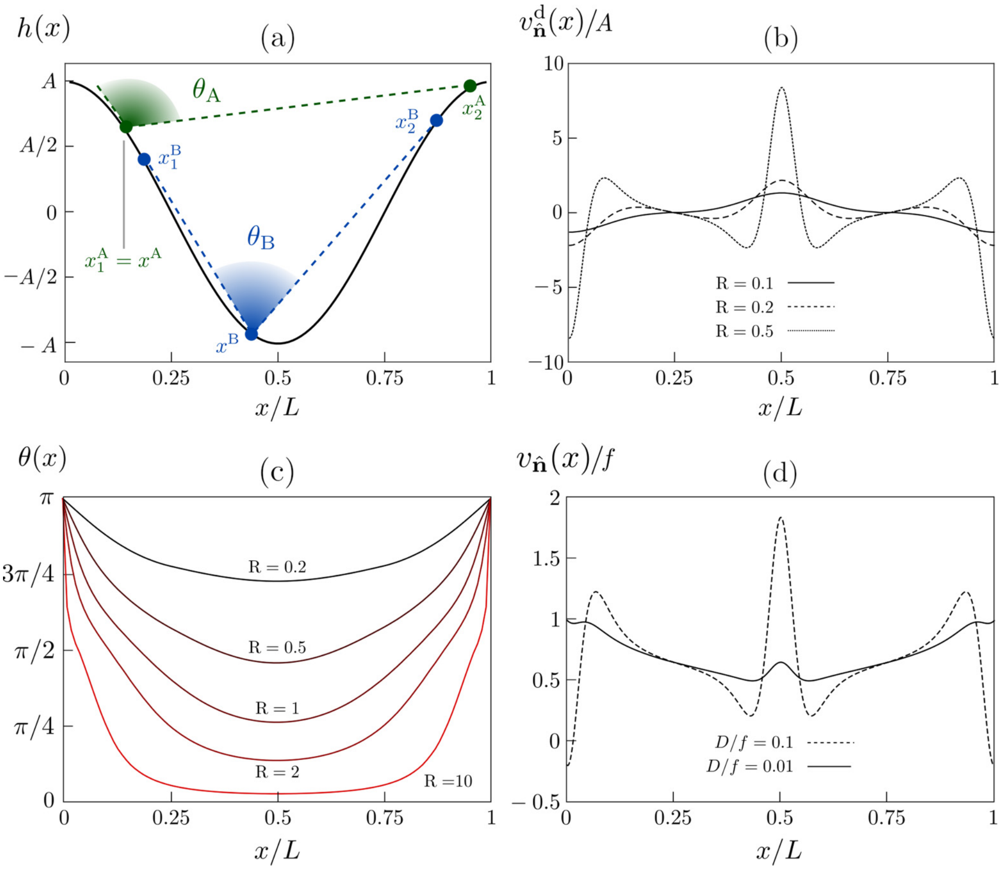

FIG. 4. Sharp-interface approach. (a) Exposure angle $\theta(x)$ for a cosine profile. Two different cases are shown: $\theta_A = \theta(x^A)$ represents the construction required when $x/L < 0.25$, where $x_1 = x$. A similar construction is expected for $x/L > 0.75$, with $x_2 = x$. $\theta_B = \theta(x^B)$ represents the case obtained for $0.25 < x/L < 0.75$, where $x_1 < x < x_2$. (b) Values of $v^d_{\hat{n}}(x)/A$ with $q = 1$ and $D = 1$ for different aspect ratios: $R = 0.1$ (solid line), $R = 0.2$ (dashed line), and $R = 0.5$ (dotted line). (c) $\theta(x)$ distribution for different R values. (d) Velocity distribution $v_{\hat{n}}(x)/f$ for a cosine with $R = 0.5$: $D = 0.1$ (solid line) and $D = 0.01$ (dashed line).

The $\hat{\boldsymbol{\tau}}_i$ vectors for profiles described by Eq. (8) are determined by considering the points x_1 and x_2 whose tangent line $\hat{\boldsymbol{\tau}}_i$ contains x without additional intersections with $h(x)$. Such a construction for the profile is illustrated in Fig. 4(a), where the two qualitatively different cases are shown. The values of the $\theta(x)$ distribution are shown in Fig. 4(c) for different values of R.

The shadowing function is defined by the exposure angle using the normalization condition:

$$S(x) = \frac{\theta(x)}{\int \theta(x) d\Gamma}. \tag{11}$$

By comparing the normal velocities due to surface diffusion $v^d_{\hat{n}}(x)$ and flux $v^f_{\hat{n}}(x)$ the competition between surface diffusion and shadowing can be investigated. In particular, we are interested here in evaluating if the amplitude of the initial profile increases, thus indicating the dominance of shadowing effects, or decreases, showing the dominance of the surface diffusion. Notice that the diffusion coefficient D directly set the local velocity $v^d_{\hat{n}}(x)$, while the parameter F set the total amount of material reaching the entire surface. In order to compare D with a parameter describing the local amount of the incoming material, the total flux density f is introduced as $f = F/L_x$ with L_x the range of x values for a 2D profile. The same would apply for a 3D profile with $f = F/(L_x L_y)$ and L_y the range of y values. This choice corresponds to normalize F by the extension of a flat surface, for which the condition $v^f_{\hat{n}}(x) = f$ is achieved everywhere. The $v_{\hat{n}}(x)$ distribution corresponding to two values of the D/f ratios are shown in Fig. 4(d).

Let us consider the velocities $v_1 = v_{\hat{n}}(0)$ and $v_2 = v_{\hat{n}}(\pi)$, representative of the evolution rate at the peaks and the valleys of the cosine profile with $q = 1$ as in Fig. 4(a). The tendency to increase or decrease the amplitude is evaluated by $\Delta v = (v_1 - v_2)/f$. Notice that this quantity corresponds also to the difference in the maximum and minimum velocity due to deposition and surface diffusion (divided by the f factor). The velocity difference Δv as function of R and D/f values, is shown in Fig. 5 (for $q = 1$). The solid red line represents the condition $v_1 = v_2$, i.e., surface diffusion and growth compensate exactly and the change in the amplitude is vanishing. Moreover, $\Delta v = 0$ condition is achieved also for vanishing R values, as $v^d_{\hat{n}}(x) = 0$ and $v^f_{\hat{n}}(x) = f$ in such a limit for any value of D/f (see $\pm 5 \times 10^{-3}$ isolines). For R values larger than 0, a positive Δv is obtained if D/f ratios are smaller than the ones corresponding to the solid red line. In this case, shadowing effects are stronger than surface diffusion leading to larger differences between the height of peaks and valleys of the surface profile, i.e., to an increasing surface roughness. Conversely, negative Δv values are obtained for larger D/f values pointing out the dominance of flattening. The information obtained by

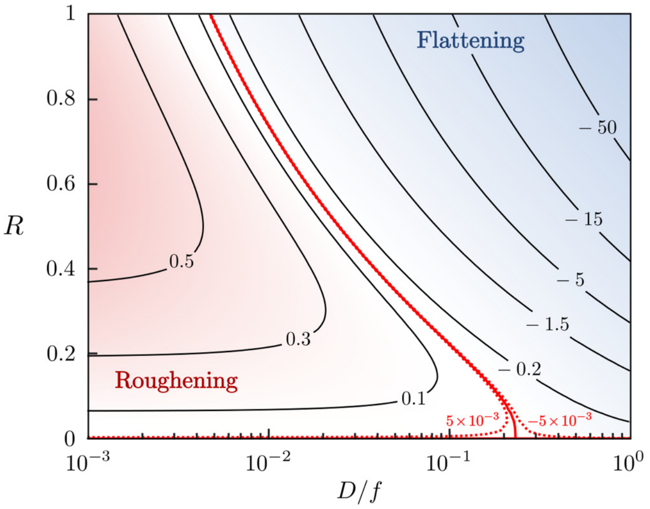

FIG. 5. Δv values as function of R and D/f for $q = 1$. Solid black lines show Δv isolines. The solid red line represents the curve at which $\Delta v = 0$, separating the region where a global smoothing is expected (flattening) from the one leading to an increasing of the surface roughness (roughening).

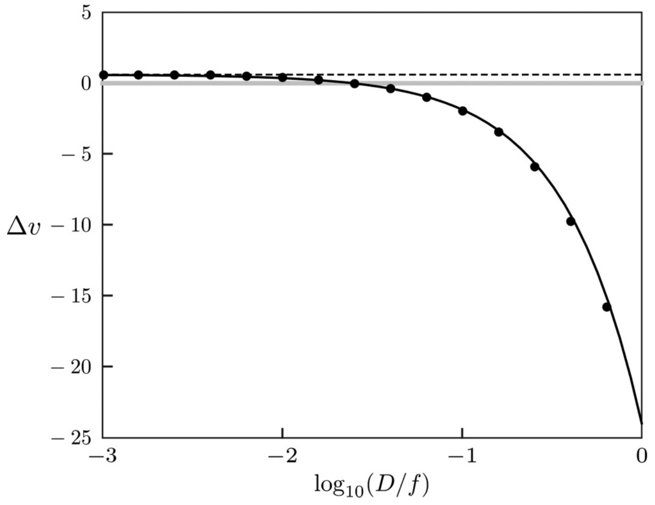

FIG. 6. Δv values, as function of the D/f ratio, in the first stages of the deposition on a cosine profile with $R = 0.5$. The results obtained by PF simulations (filled dots) and semianalytical sharp-interface approach (solid line) are reported. The value of Δv in the limit of $D \to 0$ is also shown by a dashed line.

such an analysis can be directly related to the features of the growth process. For instance, the growth temperature can be linked to the diffusion coefficient by an Arrhenius law [15]. That is, growth at high temperature would provide high values of D and vice versa. If we consider now a growth condition which provides surface roughening (i.e., in the region of Fig. 5 with $\Delta v > 0$) and the temperature is raised, the importance of surface diffusion increases and above certain values a global flattening is expected. This result is in agreement with the well-known dominance of kinetic effects for high fluxes or low temperatures along with the onset of thermodynamic regimes in the opposite case [5]. Notice that the quantitative results reported in Fig. 5 are obtained for the specific choice of the initial profile function as in Eq. (8) and they strictly refer to the first stages of the evolution. Indeed, at later stages following the very first ones, the initial profile assumes a different shape and the equations cannot be readily applied anymore. However, the plot in Fig. 5 provides an overview of the expected evolution of wavy patterned profiles and it defines a benchmark for computational approaches aiming to describe the competition between surface diffusion and shadowing effects.

B. Model assessment

The behavior obtained by simulating the evolution as described by PF equations can be directly compared to the aforementioned results. A $\varphi(\mathbf{x})$ function resembling a wavy surface as in Fig. 3 is considered, focusing on the 2D cosine profile as defined by Eq. (8). The evolution of such a surface profile is described by Eq. (2). Parameters are set to $\epsilon = \pi/10$, $\Delta x = \epsilon/8$. Moreover, hereafter the parameter controlling the amount of deposited material f is set to 1, so that the competition between shadowing and surface diffusion is controlled by means of D values, directly corresponding to D/f ratios. Random directions and initial positions of the particles for the ray-tracing algorithm are considered, simulating sputtering deposition as in Figs. 3(a)–3(c). The comparison between the results from PF simulations and the prediction of the sharp-interface approach is provided in Fig. 6, where a cosine profile with $R = 0.5$ is considered and the Δv values obtained with different D/f ratios are shown. An almost perfect agreement between the predictions of the sharp-interface model (solid line) and the PF simulation results (filled dots) is obtained. So that we can conclude that the method adopted here is able to reproduce the correct dynamics including both surface diffusion and growth with shadowing effects. While for later stages the evolution cannot be described anymore by the aforementioned semianalytical sharp-interface approach, it can be straightforwardly simulated by the PF approach as illustrated in the following section.

V. LONG-TIME-SCALE EVOLUTION

Technology-relevant processes often involve deposition on time scales well beyond the ones described by the results in Sec. IV. Indeed, a large amount of material is typically deposited to growth nano- and microstructures with significant variation of the surface morphology. In this section, the long-time-scale evolution during growth including shadowing effects and surface diffusion is investigated. Along with insights on the growth dynamics, these later stages of the growth also reveal the real strength of the approach presented in Secs. II and III.

Let us consider the cases illustrated in Fig. 3. Once the features of the deposition process are set, the impinging flux at the surface is uniquely determined by the choice of the profile. However, according to the results of the previous section, different evolutions are expected for different D/f values. In Fig. 7 the growth of the profile of Fig. 3(c) is shown for two different values of D/f. The reported profiles correspond to the $\varphi \sim 0.5$ isolines during the evolution. Four representative stages are illustrated in the different panels by

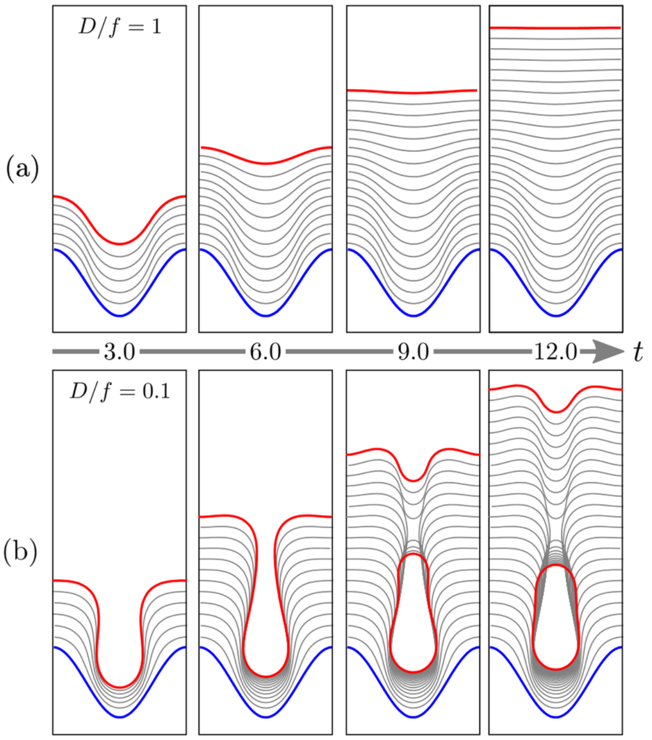

FIG. 7. PF simulations of sputtering deposition on a wavy profile: (a) $D/f = 1$ and (b) $D/f = 0.1$. Blue lines show the initial profile. Red lines correspond to the surface at the specific times reported in the figure. Δt between gray lines is 0.5.

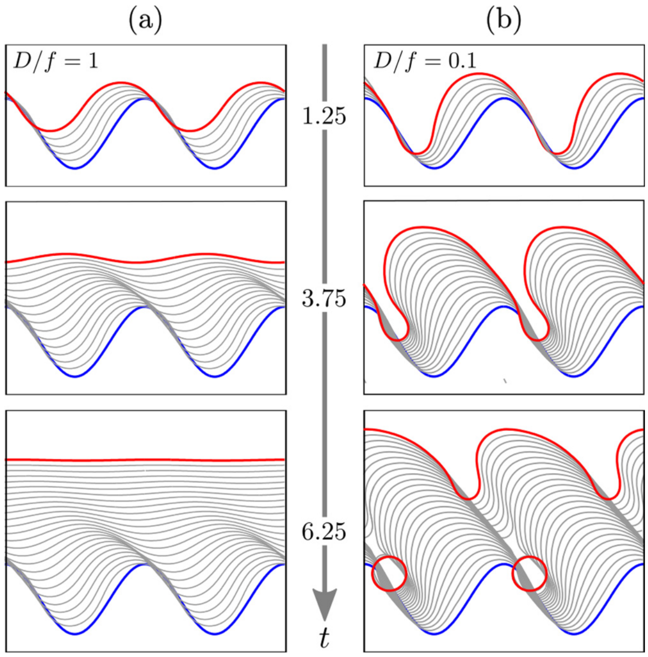

FIG. 8. PF simulations of directional deposition with $\alpha = -\pi/4$, on a wavy profile: (a) $D/f = 1$ and (b) $D/f = 0.1$. The same color code of Fig. 7 is adopted. Δt between gray lines is 0.25.

red lines. The initial profile corresponds to the blue line and intermediate stages are illustrated by gray lines. In Fig. 7(a) the D/f ratio is set to 1. An almost conformal growth is obtained in the first stages while the strong tendency towards flattening, promoted by surface diffusion, finally leads to a flat growth front. A different evolution is obtained in Fig. 7(b) with $D/f = 0.1$. While in the very early stages the amplitude of the cosine tends to decrease, as can be read from the plot in Fig. 5, the evolution of the resulting morphology at later stages shows a tendency to increase the difference between peaks and valleys. This produces the growth of columnar structures which, in turn, show an enlargement at the top with overhangs. Then, such structures are found to touch each other and holes are left in the material. Once they are formed a continuous growth front is obtained on top, and it grows according to the balance between shadowing effects and surface diffusion. The material deposition is found to be not effective within the voids as they result completely shielded. Therefore, they evolve according to surface diffusion only. Notice that, despite the presence of topological changes such as the merging of columnar structures, the entire evolution is naturally tackled by the PF approach thanks to the implicit treatment of the evolving surface.

The mechanism outlined by simulations in Fig. 7 show a good agreement with the evidence reported in the literature, concerning the growth of columnar structures when shadowing effects dominate [11,17]. Moreover, mechanisms as in Fig. 7(b) have been recently observed for the growth of vertical microstructures on deeply patterned substrates, where the key role of shadowing effects is combined to a relative high growth temperature leading to enhanced contribution of surface diffusion and merging of neighboring crystals [19]. A general qualitative description of these experimental cases is then achieved thanks to the method discussed in the previous sections. Indeed, the possibility of ranging between flat surfaces and columnar structures is demonstrated just by varying the D/f ratio. It is worth mentioning that similar behaviors were also observed and modeled for far-from-equilibrium crystalline structures during annealing, i.e., when surface diffusion is promoted by high-temperature treatments [49,50]. Here such an effect is superposed to the detailed modeling of the growth and similar results can be obtained just by setting the proper initial morphology and $F = 0$, i.e., by turning off the material deposition.

A similar investigation is also reported in Fig. 8 for the case of directional deposition as in Fig. 3(d), with the same color code as in Fig. 7. Figure 8(a) shows the evolution obtained by deposition with a prescribed direction $\alpha = -\pi/4$ for the material flux and $D/f = 1$. Isolines reveal an accumulation of material in some regions only, according to Fig. 3(d), yielding to a strongly anisotropic growth front. However, the relevance of surface diffusion is such to flatten the profile also in this case and a planar surface is finally obtained. In Fig. 8(b) a similar deposition is reported by setting $D/f = 0.1$. In this case, the material redistribution provided by surface diffusion does not lead to the flattening of the surface. Indeed, the growth of tilted structures aligned along the direction set by α is achieved. Then, also in this case, the formation of overhangs is observed with the merging of different structures along with the formation of voids. At variance with Fig. 7(b), the holes formed here are smaller, and the evolution by surface diffusion leads quickly to the equilibrium configuration, i.e., voids with a circular shape. According to the balance between deposition and surface diffusion, which is still present for the continuous profile obtained on top, the evolution is found here to form other voids, while a final flattening is obtained for the simulation in Fig. 7(b) (not shown). These results closely resemble the main features observed in the classical glancing angle deposition methods [8,9], where tilted columnar structures aligned to the direction of the flux are obtained. The nontrivial effect of surface diffusion is here superposed to the expected directional growth showing how it can affect the formation of tilted and self-aligned structures and films, along with regularly distributed holes.

The results reported in Figs. 7 and 8 reveal the main features observed during the growth on nonplanar substrates. Moreover, the more detailed features depending on the deposition flux can be identified thanks to the versatility of the considered method. In addition, notice that the specific choice of a cosine function as the initial profile is representative for the case of pit-patterned substrates [2,51,52], thus providing specific insights on such a realistic case. However, the general situation for thin films consists of a rough profile with a random height distribution. In Fig. 9 we illustrate this case by considering an initial condition set as a continuous, random profile. Moreover, to illustrate the versatility in tackling features of experiments, we set the incoming material flux to be 50% vertical, i.e., $\alpha = -\pi/2$, and 50% isotropic, i.e., $\alpha \in]-\pi\ 0[$, mimicking some peculiar growth regimes as adopted for instance in Ref. [18]. The size of the simulation domain is set here to $L_x = 12\pi$. D/f ratio is set to 0.01. The aforementioned features of the growth process are still observed here. Indeed, a smoothing of sharp peaks, where the curvature is high, is achieved in the first stages due to surface diffusion. Then, shadowing effects produce anisotropic material flux distribution which leads to different growth velocities at the surface and almost columnar structures form. Coalescence may occur during the growth of these structures forming holes within the material evolving towards circular shape according to the minimization of the surface energy.

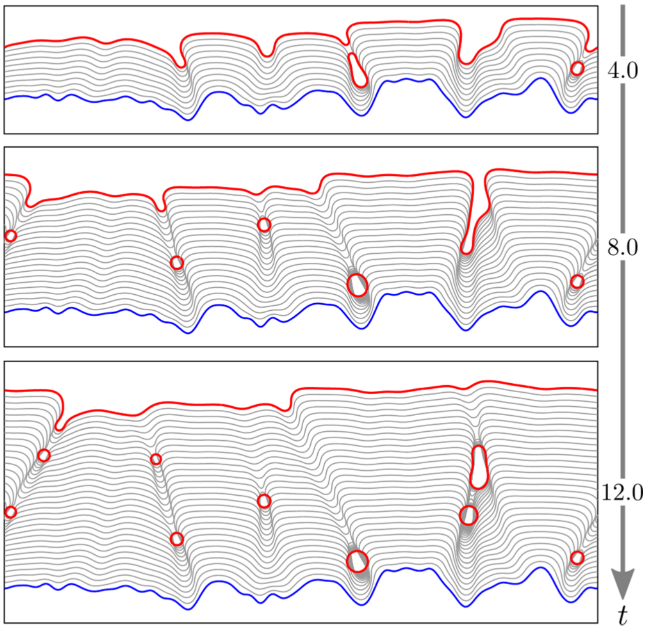

FIG. 9. Simulation of the growth on a rough profile, described by a random height distribution, with an external flux which is 50% isotropic and 50% vertical with $D/f = 0.01$. The same color code of Fig. 7 is adopted. Δt between gray lines is 0.4.

Shadowing effects tend in general to form columnar structures with elongated trenches in between when the evolution leads to an increase of the roughness, as can be seen from simulations in Figs. 7 and 8. Moreover, as can be noticed from the simulation in Fig. 9 (in between the two columnar structures on the right), if the merging of two structures forms a void with a very elongated shape, the evolution occurs with changes in the topology involving the formation of more than one hole in agreement with the expected kinetic pathway towards equilibrium provided by surface diffusion [31,34]. The formation of more than one hole between growing structures is also observed in other regions of Fig. 9. We verified that the evolution with larger diffusion coefficients suppresses the formation of voids, leading to a flat growth front also starting from the random profile considered here.

So far, only 2D results have been reported. However, the modeling of 3D geometries is highly demanded to provide comparisons with experiments and predictions on growth processes. The PF method adopted here can tackle the evolution of 3D geometries and, as already shown in Sec. III, it allows for the calculation of the flux distribution with shadowing on them. Therefore, the analysis of the evolving profile during growth can be provided also for more realistic, 3D geometries. In Fig. 10 representative cases of deposition on three-dimensional, wavy profiles are reported. In particular, Fig. 10(a) shows the evolution obtained for the 3D profile of Fig. 3(g) with $D/f = 1$. As in the corresponding 2D simulation, a quick flattening is obtained in this case revealing the dominance of surface diffusion. In Fig. 10(b) the evolution of the same profile is shown for $D/f = 0.1$. Here the contribution of surface diffusion is not enough to provide the global smoothing of the profile and peaks grow more than the deep valleys, which are present along $\langle 110 \rangle$ directions. At later stages, this produces the formation of deep pits while a network forms connecting the peaks. In contrast to the 2D simulations in Fig. 7(b) this does not lead to the formation of overhangs and topological changes. This reveals that some differences are in general expected when changing the dimensions of the system and, in particular, when accounting for the third dimension of real structures. First, the impinging material flux results from a solid view angle, thus accounting for surface corrugations in a different way. Second, surface diffusion results enhanced in 3D with respect to 2D as the curvature is given by the sum of the principal curvatures [53], so that different values are obtained for solids and for their equivalent sections in 2D [54]. Therefore, κ shows higher variations along the 3D profiles thus producing higher velocities according to Eq. (2) in the PF model or Eq. (9) in the sharp-interface approach. This effect, in particular, is responsible for the stronger surface diffusion observed in 3D which prevents the formation of overhangs for the parameters of the simulation in Fig. 10(b). In order to explore the parameter space more and provide information on this comparison, in Fig. 10(c) the evolution obtained by further decreasing the relevance of surface diffusion is reported, setting $D/f = 0.01$. Here the peaks grow significantly more

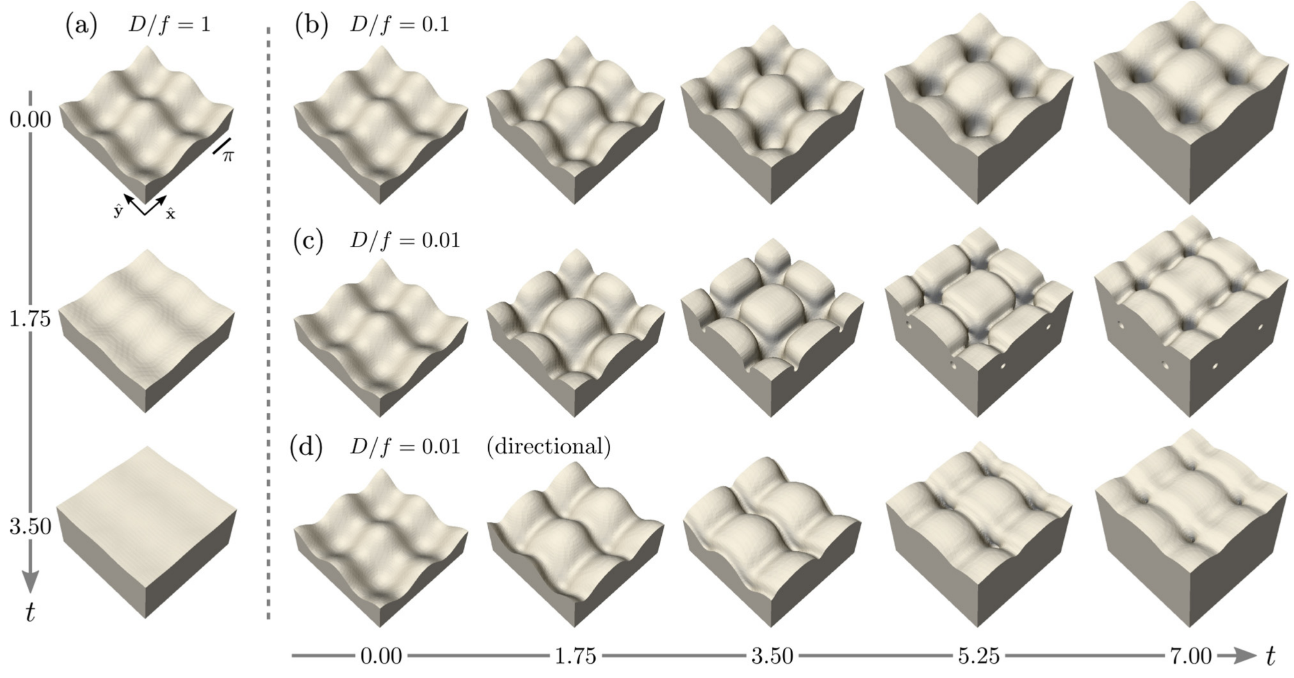

FIG. 10. Three-dimensional simulations of the growth on wavy profile. (a)–(c) Growth obtained by sputtering deposition on a profile as in Fig. 3(g) with D/f equal to 1, 0.1, and 0.01, respectively. (d) Growth obtained by directional deposition as in Fig. 3(h) with $D/f = 0.01$.

than all the other regions and they also result enlarged in shape. Then, as observed for the 2D simulations discussed above, the growing structures touch each other with the formation of holes in between and under the merged region. Notice that, due to the numerical fluctuation, the merging is not simultaneous in every direction, so that a slightly irregular profile is obtained in the last reported step. The case of a different deposition technique is also illustrated in Fig. 10(d), where the flux distribution is set as in Fig. 3(h) with $D/f = 0.01$. The growing profiles results from the larger accumulation of material on a side of the peaks in the substrate, and produces the formation of trenches in the direction perpendicular to the incoming flux orientation. Then, due to the peculiar surface morphology, overhangs form over the deepest valleys (see the profile at $t = 5.25$) and finally the merging of different regions is achieved, along with the formation of voids buried in the material.

The results reported in Fig. 10 demonstrate the applicability of the method to 3D patterned profiles, also pointing out the expected differences according to the curvature definition and the features of the flux shielding. However, they assess the outcomes of 2D simulations, reproducing similar intermediate stages during the growth. The evidence concerning flattening, roughening, or growth of columnar structures depending of the D/f ratio can then be regarded as general.

VI. CONCLUSIONS

In this work we investigated the growth dynamics of crystalline films during deposition, accounting for both surface diffusion and shadowing effects within a diffuse interface approach. The goal was achieved by exploiting a PF model of surface diffusion combined with a convenient description of the incoming material flux by a ray-tracing algorithm. The method was assessed thanks to the comparison with a sharp-interface approach describing the expected evolution in the early stages of the growth. Then, it was used to describe the later stages of the growth process when surface diffusion and shadowing effects are both relevant [11,17], e.g., during high-temperature deposition on nonflat substrates [5].

The reported simulations outline the main features of thin-film growth on undulated profiles. For high D/f ratios the dominance of surface diffusion is observed, and the dynamics towards flatting was reproduced. Moreover, the evolution towards columnar structures was described by lowering the D/f ratio. For low enough values of this quantity, the merging of neighboring structures with the formation of bridges and buried voids is also obtained. This behavior was reproduced both in 2D and 3D within the selected framework. D and f are both parameters which can be closely connected to the specific features of the growth process, namely the temperature and the amount of deposited material for a given flux distribution [5]. Then the morphological changes discussed here, and their trends by varying such parameters, are expected to be observed in experiments and they can be used to understand the results of growth process as well as to design specific morphologies by controlling the growth conditions. The direct correspondence to the outcome of specific experiments [17,19] further assess the reported investigation. Different flux distributions were also considered in order to reproduce different experimental conditions, namely sputtering and glancing-angle deposition. Despite the simulations reproduced the features of the specific processes, they also outlined the same aforementioned trends for what concerns the possible growth of columnar structures and their merging. For the sake of convenience, simple initial surfaces, described by cosine functions, were mostly adopted, still resembling the main features of profile adopted for several technological application [2,51,52]. In addition, a case dealing with a generic rough surface was also reported to confirm and extend the effectiveness of the reported results.

From the methodological point of view, a general approach for the investigations of the growth dynamics has been introduced. Indeed, it allows for the description of the impinging material flux at the surface with shadowing effects taking advantage at the same time of the well-known features of PF models, such as the easy managing of surfaces in 3D thanks to the diffuse domain approach along with the natural description of complex topological changes [31]. This coupling is proposed here and it paves the way to more comprehensive and thorough investigations of growth process on patterned substrates (see, e.g., Refs. [8,9,18]). Moreover, it is also worth mentioning that more complex scenarios can be present during crystal growth, e.g., showing crystal faceting and/or elastic energy minimization [5]. These effects are known to be described by PF models [7,34,36,55], which are compatible with the one reported in Sec. II. So that the shadowing calculations provided here can be used for several other investigations.

Future studies will be devoted to the extension of the analysis reported in this work to the growth dynamics of thin films when deposited on more complex patterned substrates. Moreover, an interesting perspective consists in driving the self-assembly of voids in ordered arrays by exploiting the aforementioned mechanisms and the reported simulation technique.

ACKNOWLEDGMENTS

We kindly acknowledge F. Stenger (TU-Dresden) and R. Bergamaschini (University of Milano-Bicocca) for fruitful discussions. We also thank Professor F. Montalenti and Professor L. Miglio (University of Milano-Bicocca), who first pointed out to us the importance of shadowing effects during the deposition on nonplanar substrates. M.S. acknowledges the support of the Postdoctoral Research Fellowship awarded by the Alexander von Humboldt Foundation. The computational resources were provided by ZIH at TU Dresden and by the Jülich Supercomputing Center within the Project No. HDR06.

[1] V. Shchukin and D. Bimberg, Rev. Mod. Phys. **71**, 1125 (1999).
[2] J. Stangl, V. Holý, and G. Bauer, Rev. Mod. Phys. **76**, 725 (2004).
[3] J.-N. Aqua, I. Berbezier, L. Favre, T. Frisch, and A. Ronda, Phys. Rep. **522**, 59 (2013).
[4] C. V. Falub, H. von Kanel, F. Isa, R. Bergamaschini, A. Marzegalli, D. Chrastina, G. Isella, E. Muller, P. Niedermann, and L. Miglio, Science **335**, 1330 (2012).
[5] A. Pimpinelli and J. Villain, *Physics of Crystal Growth* (Cambridge University Press, Cambridge, 1998).
[6] P. Politi, G. Grenet, A. Marty, A. Ponchet, and J. Villain, Phys. Rep. **324**, 271 (2000).
[7] R. Bergamaschini, M. Salvalaglio, R. Backofen, A. Voigt, and F. Montalenti, Adv. Phys. X **1**, 331 (2016).
[8] M. M. Hawkeye and M. J. Brett, J. Vac. Sci. Technol. A **25**, 1317 (2007).
[9] A. Barranco, A. Borras, A. R. Gonzalez-Elipe, and A. Palmero, Prog. Mater. Sci. **76**, 59 (2016).
[10] R. P. U. Karunasiri, R. Bruinsma, and J. Rudnick, Phys. Rev. Lett. **62**, 788 (1989).
[11] G. S. Bales, J. Vac. Sci. Technol. A **9**, 145 (1991).
[12] G. S. Bales and A. Zangwill, Phys. Rev. Lett. **63**, 692 (1989).
[13] C. Roland and H. Guo, Phys. Rev. Lett. **66**, 2104 (1991).
[14] J. H. Yao and H. Guo, Phys. Rev. E **47**, 1007 (1993).
[15] W. W. Mullins, J. Appl. Phys. **28**, 333 (1957).
[16] W. W. Mullins, J. Appl. Phys. **30**, 77 (1959).
[17] G. S. Bales, R. Bruinsma, E. A. Eklund, R. P. U. Karunasiri, J. Rudnick, and A. Zangwill, Science **249**, 264 (1990).
[18] R. Bergamaschini, F. Isa, C. Falub, P. Niedermann, E. Müller, G. Isella, H. von Knel, and L. Miglio, Surf. Sci. Rep. **68**, 390 (2013).
[19] R. Bergamaschini, M. Salvalaglio, A. Scaccabarozzi, F. Isa, C. V. Falub, G. Isella, H. von Känel, F. Montalenti, and L. Miglio, J. Cryst. Growth **440**, 86 (2016).
[20] M. F. Castez, R. C. Salvarezza, and H. G. Solari, Phys. Rev. E **73**, 011607 (2006).
[21] T. H. Vo Thi, J.-L. Rouet, P. Brault, J.-M. Bauchire, S. Cordier, and C. Josserand, J. Phys. D **41**, 022003 (2008).
[22] J. Krug and P. Meakin, Phys. Rev. E **47**, R17 (1993).
[23] J. T. Drotar, Y.-P. Zhao, T.-M. Lu, and G.-C. Wang, Phys. Rev. B **62**, 2118 (2000).
[24] T. Karabacak, H. Guclu, and M. Yuksel, Phys. Rev. B **79**, 195418 (2009).
[25] T. Karabacak, J. Nanophoton. **5**, 052501 (2011).
[26] J. Krug, Adv. Phys. **46**, 139 (1997).
[27] D. Adalsteinsson and J. A. Sethian, J. Comput. Phys. **120**, 128 (1995).
[28] D. Adalsteinsson and J. A. Sethian, J. Comput. Phys. **122**, 348 (1995).
[29] O. Ertl and S. Selberherr, Microelectron. Eng. **87**, 20 (2010).
[30] L.-Q. Chen, Annu. Rev. Mater. Res. **32**, 113 (2002).
[31] B. Li, J. Lowengrub, A. Ratz, and A. Voigt, Commun. Comput. Phys. **6**, 433 (2009).
[32] I. Steinbach, Model. Simul. Mater. Sc. **17**, 073001 (2009).
[33] S. Torabi, J. Lowengrub, A. Voigt, and S. Wise, Proc. R. Soc. London Ser. A **465**, 1337 (2009).
[34] M. Salvalaglio, R. Backofen, R. Bergamaschini, F. Montalenti, and A. Voigt, Crystal Growth Design **15**, 2787 (2015).
[35] M. Salvalaglio, R. Bergamaschini, R. Backofen, A. Voigt, F. Montalenti, and L. Miglio, Appl. Surf. Sci. **391**, 33 (2017).
[36] A. Rätz, A. Ribalta, and A. Voigt, J. Comput. Phys. **214**, 187 (2006).
[37] M. Albani, R. Bergamaschini, and F. Montalenti, Phys. Rev. B **94**, 075303 (2016).
[38] R. Backofen, R. Bergamaschini, and A. Voigt, Philos. Mag. **94**, 2162 (2014).
[39] W. Jiang, W. Bao, C. V. Thompson, and D. J. Srolovitz, Acta Mater. **60**, 5578 (2012).
[40] C. Gugenberger, R. Spatschek, and K. Kassner, Phys. Rev. E **78**, 016703 (2008).
[41] A. Voigt, Appl. Phys. Lett. **108**, 036101 (2016).
[42] S. Vey and A. Voigt, Comput. Visual. Sci. **10**, 57 (2007).

[43] T. Witkowski, S. Ling, S. Praetorius, and A. Voigt, Adv. Comput. Math. **41**, 1145 (2015).

[44] A. S. Glassner, *An Introduction to Ray Tracing* (Morgan Kaufmann, San Francisco, 1989).

[45] M. Pharr, W. Jakob, and G. Humphreys, *Physically Based Rendering: From Theory to Implementation*, 3rd ed. (Morgan Kaufmann, San Francisco, 2016).

[46] We use the standard definition of nearest neighbors. That is, four neighboring cells in 2D and six neighboring cells in 3D.

[47] J. A. Sethian and P. Smereka, Annu. Rev. Fluid Mech. **35**, 341 (2003).

[48] Notice that in the limit of small amplitudes the well known approximation $\kappa(x) \approx -h''(x) = q^2 A\cos(qx)$ is obtained and $v^{\mathrm{d}}_{\hat{\mathbf{n}}} \approx -q^4 A\cos(qx)$. However, we are interested in evaluating the evolution of surface corrugations which have large values of A compared to the ones where the small amplitude approximation can be adopted so that the evaluation of Eq. (9) has to be considered.

[49] M. Salvalaglio, R. Bergamaschini, F. Isa, A. Scaccabarozzi, G. Isella, R. Backofen, A. Voigt, F. Montalenti, G. Capellini, T. Schroeder, H. von Känel, and L. Miglio, ACS Appl. Mater. Interfaces **7**, 19219 (2015).

[50] A. Kosinova, D. Wang, P. Schaaf, O. Kovalenko, L. Klinger, and E. Rabkin, Acta Mater **102**, 108 (2016).

[51] G. Biasiol and E. Kapon, Phys. Rev. Lett. **81**, 2962 (1998).

[52] R. Bergamaschini, J. Tersoff, Y. Tu, J. J. Zhang, G. Bauer, and F. Montalenti, Phys. Rev. Lett. **109**, 156101 (2012).

[53] J. W. Cahn and D. W. Hoffman, Acta Metall. **22**, 1205 (1974).

[54] For instance, a 3D sphere has a doubled curvature than a 2D circle with the same radius.

[55] L. K. Aagesen, M. E. Coltrin, J. Han, and K. Thornton, J. Appl. Phys. **117**, 194302 (2015).